**Atmospheric
Measurement
Techniques**

Observation of strato-mesospheric CO above Kiruna with ground-based microwave radiometry – retrieval and satellite comparison

C. G. Hoffmann[1], U. Raffalski[2], M. Palm[1], B. Funke[3], S. H. W. Golchert[1], G. Hochschild[4], and J. Notholt[1]

[1]Institute of Environmental Physics, University Bremen, Bremen, Germany
[2]Swedish Institute of Space Physics, Kiruna, Sweden
[3]Instituto de Astrofísica de Andalucía, CSIC, Granada, Spain
[4]Institute for Meteorology and Climate Research, Karlsruhe Institute of Technology, Karlsruhe, Germany

Abstract. CO serves as a tracer for dynamics in the polar winter middle atmosphere. This work presents the retrieval and the characterization of ground-based CO measurements from the winters 2008/2009 and 2009/2010 by the Kiruna microwave radiometer KIMRA, located in northern Sweden (67.8° N, 20.4° E). Furthermore, the dataset is used for an extensive comparison to the recent satellite instruments MLS on Aura, ACE-FTS, and MIPAS on Envisat.

The vmr profiles are retrieved using the optimal estimation approach. A detailed analysis of the averaging kernel functions is carried out, showing sensitivity of the measurements between 40 and 80 km altitude, a vertical resolution of 16 to 22 km, as well as a residual influence of the region up to 130 km altitude. An error assessment reveals a total error of the retrieved profile that increases with altitude and is approx. ± 0.1 ppmv at 50 km altitude and ± 3 ppmv at 80 km altitude. The main contributions to this total error arise from the measurement noise and the uncertainty of the used temperature profiles. The expected dynamical features of the polar winter middle atmosphere are qualitatively identified in the retrieved time series, but are not quantitatively analyzed here.

The dense MLS dataset is used to investigate the influence of the collocation criteria on the satellite comparison, showing that relaxing the distance criterion causes a high bias for MLS. The comparison including the other instruments is difficult because of the small number of coincidences. However, it suggests that there is a general agreement between KIMRA and the satellite instruments below 65 km altitude, but a high bias for KIMRA above this altitude. Furthermore, the shape of the KIMRA profile appears to be systematically different from the satellite profiles.

1 Introduction

Carbon monoxide (CO) is a good tracer for dynamical processes in the middle atmosphere during polar night, first, because of its long chemical lifetime, and second, because of a strong increase in its volume mixing ratio (vmr) in the mesosphere and lower thermosphere (MLT) region. This strong vertical gradient, which allows tracking of vertical motions, is the result of CO production by the photolysis of CO_2 in the MLT region and CO destruction by a reaction with OH in the stratosphere (e.g. Solomon et al., 1985).

The dynamical situation of the middle atmosphere in the winter hemisphere is dominated by a strong zonal westerly wind band, forming the polar vortex, which separates polar air masses from the mid-latitudes. The meridional circulation is directed toward the winter pole, resulting in convergence and descent of air masses above the pole (e.g. Holton and Alexander, 2000). Dynamics in the middle atmosphere exhibit a strong variability on different timescales, introducing variability in other atmospheric parameters, e.g. in stratospheric ozone abundances. One pronounced example of interseasonal variability are sudden stratospheric warmings (SSW), during which the polar vortex may break down completely (e.g. Labitzke and van Loon, 1999; Manney et al.,

2009). The tracer CO is a useful tool to study the different dynamical processes involved.

Since CO has a simple rotational spectrum in the microwave region with approximately equally spaced lines every 115 GHz, it can be observed using microwave radiometry. Emission spectra and respective vmr profiles of mesospheric CO have already been obtained by Waters et al. (1976); Goldsmith et al. (1979); Künzi and Carlson (1982). Since then, a number of ground-based microwave radiometers have been developed and used for studies covering various time periods in several locations, demonstrating the potential of analyses of CO datasets (e.g. Bevilacqua et al., 1985; Aellig et al., 1995; Forkman et al., 2003; Di Biagio et al., 2010).

In addition to the microwave technique, ground-based Fourier transform infrared spectrometry has also been applied in the study of strato-mesospheric CO (Kasai et al., 2005). With this technique, long term datasets have already been obtained and analysed (Velazco et al., 2007; Borsdorff and Sussmann, 2009); however, this technique is limited to sunny weather conditions and the measurement of the strato-mesospheric CO column.

In parallel to the development of ground-based measurements, satellite observations of strato-mesospheric CO have also been established (e.g. López-Valverde et al., 1993; Dupuy et al., 2004; Filipiak et al., 2005; Clerbaux et al., 2008; Funke et al., 2009). In contrast to ground-based measurements, which provide a high temporal and horizontal resolution at the measurement location, the advantage of satellite observations is good spatial coverage, and therefore a global view on CO abundances.

In this paper we present the first two winters (2008/2009 and 2009/2010) of the ongoing CO measurements by the ground-based microwave radiometer KIMRA in Kiruna, Sweden, as well as an intercomparison with three recent satellite instruments. In Sect. 2, we briefly introduce the instrument and the obtained dataset. In Sect. 3, we describe the retrieval of the vmr profiles together with a detailed analysis of the retrieval performance and an error estimation. Sect. 4 contains a brief discussion of the obtained CO vmr time series and in Sect. 5 the satellite comparison is presented.

2 Instrument and dataset

2.1 Measurement location

The observations are carried out in Kiruna, northern Sweden (67.8° N, 20.4° E, 425 m elevation) in the labs of the Swedish Institute of Space Physics (Institutet för rymdfysik, IRF). During the winter season, the state of the middle atmosphere above this location is mainly given by polar vortex conditions. However, Kiruna is close to the Arctic circle and the vortex boundary may cross the measurement location several times during a winter season, so that mid-latitude air may be measured (Raffalski et al., 2005). This will demand a careful separation of these periods in the scientific interpretation of the dataset but it also gives opportunities like to compare different air masses in a continuous dataset or to investigate the timing of the overpasses in models.

2.2 Instrument

The Kiruna Microwave Radiometer KIMRA is a joint venture of the IRF and the Institute for Meteorology and Climate Research, Karlsruhe Institute of Technology (KIT). KIMRA contains a cryogenically cooled conventional Schottky diode mixer and has a receiver noise temperature of about 1800 K in single side band (SSB) mode. KIMRA covers the frequency range from 195 to 234 GHz and has been operated at IRF Kiruna since 2002.

The observations are performed according to the reference beam-method suggested by Parrish et al. (1988). However, for the reference beam and the balanced calibration an internal adjustable reference load (Berg et al., 1998) is used.

KIMRA has a periscope-like mirror system, which allows for observations with an azimuth angle between 0° and 360° as well as with an elevation angle between 0° and 90° (horizontal to vertical). The azimuth angles of all the observations in this work are either 0° or 180°, whereas the optimal elevation angle is automatically chosen according to the tropospheric transmissivity. In case of a change of the tropospheric conditions, the ongoing observation is stopped and a new measurement is automatically started, using the new optimal elevation angle. Therefore the integration time per spectrum varies between approx. 30 and 360 min. All spectra obtained are generally saved without any further quality check at the time of the measurement and are sorted later in the retrieval process according to the particular requirements.

In a first period of operation from 2002 until 2007 only O_3 measurements have been performed (Raffalski et al., 2005) using a wide-band acusto-optical spectrometer (AOS, bandwidth 1.2 GHz, 2048 channels). Data of this period was used for the validation of the GOMOS (Meijer et al., 2004) and MIPAS (Steck et al., 2007) instruments on board the satellite ENVISAT.

In 2007, KIMRA was extended to be capable of measuring strato-mesospheric CO simultaneously with O_3 (see Fig. 1 for an overview of the spectral region). For this, a high-resolution Fast-Fourier-Transform spectrometer (FFTS, bandwidth 110 MHz, 1024 channels) was included, which is able to resolve the narrow CO emission line at 230 GHz. Since then, KIMRA is routinely operated with both spectrometers in parallel. The present study of CO is, however, focused on the high-resolution spectra (Fig. 2, top panel), obtained with the FFTS.
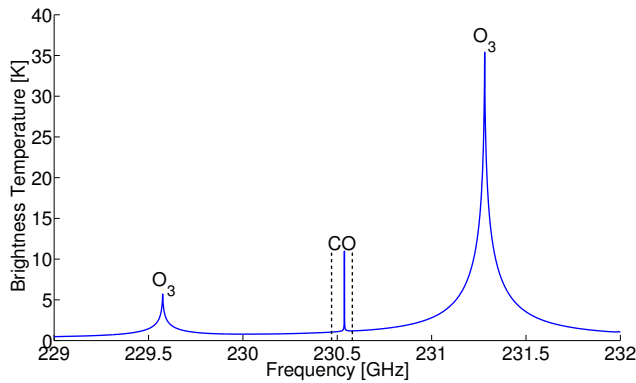
Fig. 1. Sketch of the emission lines in the spectral region around the CO line of interest calculated with ARTS to visualize the line positions. The black dashed lines indicate the spectral region covered by the FFT spectrometer. Continuum emission has been omitted in the calculation of this plot.

2.3 Dataset

Operational measurements have been performed since the end of the year 2008, so that the obtained spectra cover the winter 2008/2009 from December 2008 on and the full winter 2009/2010. In principle, data for the winter 2007/2008 are also available, but due to the experimental state of the instrument during that time, the desired data quality cannot be guaranteed.

One winter of continuous measurements is considered to last from September to April. However, periods of instrument maintenance and bad weather conditions may cause interruptions of several days to weeks. The measurements from the summer months are generally not analyzed since the increased humidity causes the background radiation to be too high for reasonable CO retrievals.

The signal-to-noise ratio varies from spectrum to spectrum due to both changes in the atmosphere (humidity and CO itself) and changes of instrument parameters (elevation angle, azimuth angle and the integration time; Sect. 2.2). A quality check is applied before retrieving the spectra, which was adjusted in tests under consideration of different criteria (total integration time, ratio of atmospheric and calibration integration time, spikes in spectra, noise).

In total 1497 spectra were retrieved, which are distributed over 309 days in the measurement period and have a mean atmospheric integration time of approx. 1 h. Further characteristics of this subset of spectra are summarized in Table 1. Note that due to the change of the elevation angle between single measurements, spectra cannot be averaged to produce spectra with a uniform integration time. The spectra are therefore retrieved as they are and the profiles may be averaged afterwards if necessary. The change of the azimuth angle is not relevant for the retrieval but may be considered in detailed analyses of the obtained profiles.

Table 1. Characteristics of the measurements.

Period	Dec 2008–Apr 2009
	Sep 2009–Apr 2010
Days covered	309 of 393
Total number of spectra	1497
Mean number on measurements per day	3.8
Mean integration time per spectrum	59 ± 20 min
Mean noise on spectra	0.20 ± 0.04 K
Mean elevation angle	$30° \pm 15°$
Min/Max elevation angle	$5°/90°$
Number of spectra with azimuth $180°$	802
Number of spectra with azimuth $0°$	695

3 Retrieval of vertical profiles

3.1 Theory

The retrieval of a vertical profile from a measured microwave spectrum is based upon the pressure broadening of the respective emission line. The derivation of the profile is achieved by an inversion of the forward model $\boldsymbol{F}$. It simulates a spectrum $\boldsymbol{y}$, which would have been measured if the atmosphere had a given state $\boldsymbol{x}$.

$$\boldsymbol{y} = \boldsymbol{F}(\boldsymbol{x}) + \boldsymbol{\epsilon} \qquad (1)$$

where $\boldsymbol{\epsilon}$ represents the measurement noise. The assumed atmospheric state $\boldsymbol{x}$ is then iteratively modified until the simulated spectrum fits the measured one. However, this implicit inversion of the forward model is an ill-posed problem, so that a regularization is necessary to find an appropriate solution.

The regularization approach used here is the optimal estimation (OE) method, which has been described extensively in Rodgers (2000). In OE, statistical a priori knowledge about the state of the atmosphere is used to constrain the solution. In particular, a Gaussian distribution with mean $\boldsymbol{x}_a$, the a priori profile, and the corresponding a priori covariance matrix $\mathbf{S}_a$ of the respective species are used. The fact that the measured spectrum $\boldsymbol{y}$ is affected by measurement noise $\boldsymbol{\epsilon}$, is reflected by the inclusion of the measurement noise covariance matrix $\mathbf{S}_\epsilon$.

The best estimator $\widehat{\boldsymbol{x}}$ for the true atmospheric state in OE is then found by minimizing the expression

$$[\boldsymbol{y} - \boldsymbol{F}(\boldsymbol{x})]^T \, \mathbf{S}_\epsilon^{-1} [\boldsymbol{y} - \boldsymbol{F}(\boldsymbol{x})] + [\boldsymbol{x} - \boldsymbol{x}_a]^T \, \mathbf{S}_a^{-1} [\boldsymbol{x} - \boldsymbol{x}_a]. \quad (2)$$

After the iteration, $\widehat{\boldsymbol{x}}$ can be expressed as

$$\widehat{\boldsymbol{x}} = \boldsymbol{x}_a + \mathbf{D}(\boldsymbol{y} - \mathbf{K}\boldsymbol{x}_a) \qquad (3)$$

with the Jacobian of the forward model $\mathbf{K}$ and the "contribution function matrix" $\mathbf{D}$:

$$\mathbf{D} = \left(\mathbf{K}^T \, \mathbf{S}_\epsilon^{-1} \, \mathbf{K} + \mathbf{S}_a^{-1} \right)^{-1} \mathbf{K}^T \, \mathbf{S}_\epsilon^{-1}. \qquad (4)$$

Information on the measurement sensitivity and vertical resolution is contained in the "averaging kernel" (AVK) matrix $\mathbf{A}$, which relates changes in the true state $\boldsymbol{x}$ and the retrieved state $\hat{\boldsymbol{x}}$:

$$\mathbf{A} = \frac{\partial \hat{\boldsymbol{x}}}{\partial \boldsymbol{x}} = \mathbf{D}\,\mathbf{K}. \tag{5}$$

The AVK for a particular altitude z^i is contained in the respective row $A^{i\cdot}$ of the AVK matrix $\mathbf{A}$. It is a measure for the sensitivity of the retrieved value $\hat{x}^i$ to perturbations of the true state in any single altitude considered in the retrieval. $\mathbf{A}$ usually deviates from the identity matrix, reflecting the limited altitude resolution of the retrieval. The retrieved profile is not only governed by the atmospheric state but also by both the instrumental properties and the a priori, so that the relationship between the retrieved and the true state is given by the transfer function

$$\hat{\boldsymbol{x}} = \boldsymbol{x}_\mathrm{a} + \mathbf{A}(\boldsymbol{x} - \boldsymbol{x}_\mathrm{a}). \tag{6}$$

Equation (6) is also used to compare the retrieved profiles with vertically better resolved measurements, assuming that the independent measurement represents the true state $\boldsymbol{x}$.

3.2 Retrieval setup

In this paper, the first operational version of the retrieval of the KIMRA CO spectra, called KIMRA CO version 1.1, is presented. It was developed and performed by the Institute of Environmental Physics, University of Bremen (IUP).

The forward model for the radiative transfer used in this study is the atmospheric radiative transfer simulator, ARTS, version 1.0.216 (Bühler et al., 2005). For the inversion with OE, the tool Qpack, version 1.0.93, is used (Eriksson et al., 2005). Besides the CO emission line of interest at 230.5 GHz, ozone lines in this spectral region are also modeled to account for their influence on the baseline (Fig. 1). Furthermore, the continuum absorption of H_2O, O_2, and N_2 is accounted by inclusion of the MPM93 absorption model (Bühler et al., 2005, and references therein). The line parameters as input for the forward model are taken from the HITRAN 2004 spectroscopic database (Rothman et al., 2005).

Pressure- and temperature profiles needed as input for the retrieval have generally been taken from the SABER satellite instrument (Remsberg et al., 2008). Only the lower part up to 17 km altitude comes from ECMWF Operational Analyses data. This is in contrast to the retrieval of ozone performed at IUP (Palm et al., 2010), for which ECMWF data with a static extension in higher altitudes are used. The latter turned out to be insufficient for the CO retrieval because of the greater importance of contributions from the lower thermosphere to the CO emission. The SABER profiles within a collocation box from 50° N to 75° N latitude and 15° E to 25° E longitude have been averaged daily prior to the use in the retrieval. The collocation box extends so far south because the northern edge of the SABER coverage changes from 83° N (north

viewing mode) to 52° N (south viewing mode) approx. every 60 days (Remsberg et al., 2008). Thus, during periods with usage of the south viewing mode, only the southernmost part of the chosen collocation box contains profiles. A possible bias caused by this fact has been considered in the error assessment (Sect. 3.5.2). Note that the use of SABER temperature data as retrieval input has the disadvantage, that the presented KIMRA CO retrieval cannot be performed continuously in future after SABER is not operational anymore. Therefore it is intended to use other temperature datasets, once a consistent long-term time series of the KIMRA CO is of interest. The presented dataset, serves in this case as standard to assess the influence of different temperature data. However, the present application of the retrieved time series are dynamical studies of the available period, for which the use of the SABER dataset is the best choice.

The a priori profiles of CO (Fig. 3), as well as O_3, O_2, and H_2O are based on a run of the Whole Atmosphere Community Climate Model (WACCM) (Garcia et al., 2007), which was provided by Douglas Kinnison, National Center for Atmospheric Research (NCAR), Boulder, USA. An averaged profile over a complete modeled winter is used as a priori for the complete retrieved time series. This gives the confidence that all the variations in CO seen in the time series (Sect. 4) come from the measurement alone. The used N_2 abundance is taken from the FASCOD subarctic winter scenario (Anderson et al., 1986). The a priori covariance matrix $\mathbf{S}_\mathrm{a}$ has initially been based on the respective WACCM CO standard deviation, but was then empirically modified to give the retrieval enough freedom to fit the spectra of the whole course of the winter sufficiently. Major changes have thereby been made above 80 km altitude, where the available information on the CO statistics is least certain. Non-diagonal elements are zero, thus possible correlations between vertical layers are not considered. Like the a priori profiles, $\mathbf{S}_\mathrm{a}$ is also left constant for the complete retrieval run. It is defined in fractions of the a priori on the retrieval grid. The diagonal elements converted to absolute vmr $\sqrt{S_\mathrm{a}^{ii}} \cdot x_\mathrm{a}^i$ are shown in Fig. 3, red dashed curve. The noise covariance matrix $\mathbf{S}_\epsilon$ is calculated for each spectrum from the noise in a region that only contains the background signal.

Furthermore, the retrieval accounts for instrumental artifacts, which cannot completely be suppressed during the measurements. In particular, the magnitude of standing waves is fitted, which are undulations of the spectrum baseline that arise from minor reflections in the instrument optics. Generally, this can be challenging, since it is often difficult to distinguish these standing waves from the actual emission line. In the present case, however, the emission line is much smaller than the spectral bandwidth, so that large parts of the spectrum directly show the disturbed baseline and can be used to identify the standing waves. Additionally, the standing waves have relatively large wavelengths, so that they are distinguishable from the emission line. Three different wavelengths (55 MHz, 36.6 MHz and 27.5 MHz) are fitted
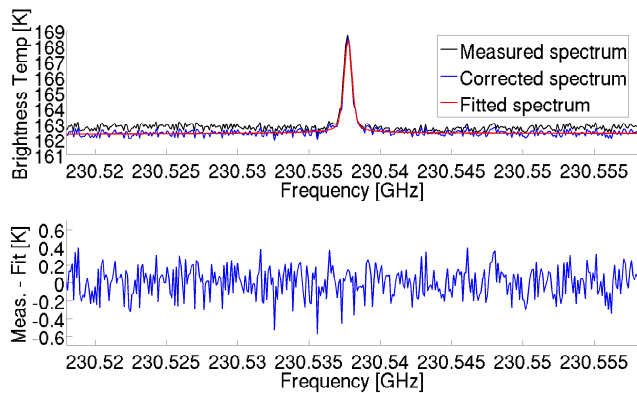
Fig. 2. Top panel: spectrum measured on 29 October 2009, 06:52 h (black) and the same spectrum corrected for standing waves (blue), together with the fit calculated by the retrieval process (red). Bottom: the corresponding residuum (difference of the corrected spectrum and the fitted spectrum), which contains only noise contributions, showing that the CO line was fitted adequately.

Fig. 3. Retrieved CO profiles (selected to cover the complete range of the CO change during a winter), as well as the constant a priori profile and its assumed standard deviation represented by $\sqrt{S_a^{ii}} \cdot x_a^i$. The range of sensitivity of the KIMRA CO measurements (Sect. 3.4) is marked with black dashed lines. Out of this range the profiles are not reliable, but are shown here for a complete demonstration of the retrieval results.

with resulting amplitudes of approximately 0.1 K. Likewise, a baseline offset of the order of about 1 K is fitted.

The retrieval is performed on a pressure grid that corresponds to fixed altitudes with 1 km spacing between 0.5 km and 130.5 km, which is much more narrow than the actual vertical resolution of the measurement. Such a narrow grid is used to gain numerical stability of the retrieval although it may cause spurious structures of smaller vertical extent in the retrieved profile, which do not have a representation in the real atmosphere (Sect. 3.3). However, this is unproblematic, since the real vertical information content is given by the AVK functions (Sect. 3.4).

In order to deal with the strong gradient in the CO vmr, the retrieved quantity is the profile $\hat{x}_{frac}$ in fractions of the a priori x_a, instead of the vmr profile $\hat{x}_{vmr}$ itself:

$$\hat{x}^i = \hat{x}_{frac}^i = \frac{\hat{x}_{vmr}^i}{x_a^i}. \tag{7}$$

The gained AVK matrix also corresponds to the fractional profiles ($\mathbf{A} = \mathbf{A}_{frac}$) and has to be converted to be representative for the vmr profile

$$A_{vmr}^{ij} = x_a^i \cdot A_{frac}^{ij}/x_a^j. \tag{8}$$

In the following, the short terms "fractional AVK" matrix and "vmr AVK" matrix are used to refer to $\mathbf{A}_{frac}$ and $\mathbf{A}_{vmr}$ respectively, although both representations are dimensionless.

3.3 Typical retrieval results

The retrieval result of 29 October 2009, 06:52 h, is a typical example of the retrieved dataset in the sense that the values for the integration time and the elevation angle of the selected spectrum are close to the mean values of the complete data set. The spectrum (Fig. 2, top panel) is fitted adequately by
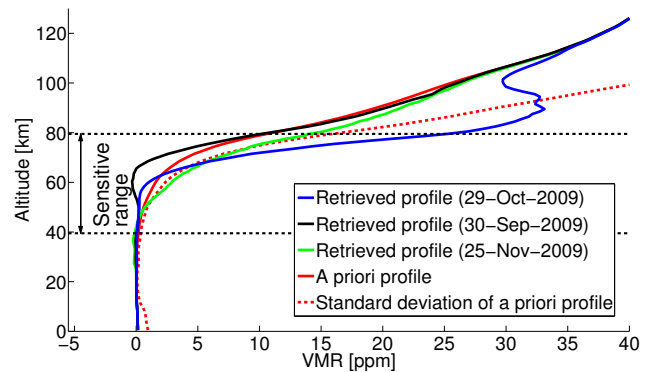
the retrieval process, so that the residuum (Fig. 2, bottom panel) contains only the noise contribution.

The respective profile and the constant a priori are shown (together with two more example profiles) on the retrieval grid over the full altitude range (Fig. 3), albeit the sensitive vertical range is located between 40 and 80 km with a vertical resolution of approx. 20 km (Sect. 3.4). With that, the interesting part of the profile, the steep increase of CO in the mesosphere, is covered. As expected, the retrieved profiles tend toward the a priori as the sensitivity above the meaningful range decreases.

Note that at the location of the transition from low CO to the steep increase, a small negative overshoot may be retrieved (Fig. 3, profile of 30 September 2009 at about 60 km). Although being an unphysical result, this behavior is unproblematic since the vertical extent of the negative vmr is smaller than the vertical resolution of the measurement (Sect. 3.4). Thus it is an example for possible artifacts produced by the narrow retrieval grid as mentioned in Sect. 3.2.

3.4 Performance of the retrieval

To specify the performance of the retrieval, particular properties of the AVK matrix (Eq. 5) are examined in the following according to Rodgers (2000). It will be shown, that the retrieval works generally reasonable between 40 and 80 km with a vertical resolution of 16 to 22 km. However, the region between 70 and 80 km has to be treated with care depending on the particular application.

Note that the performance varies from profile to profile since the signal-to-noise ratio, which determines the information content, is not constant (Sect. 2.3). Therefore general properties of the AVKs, calculated as averages over the

whole dataset, are discussed first, before a typical set of AVKs is shown in Sect. 3.4.5.

Note further that the retrieval performance is not compared here to previous studies mentioned in the introduction. Although this could generally be an additional indication for the functioning of the of the developed retrieval setup, it is not necessarily conclusive, since many properties (integration time, receiver noise temperature, measured CO transition, spectral resolution) of the underlying measured spectra differ significantly, which is expected to influence the retrieval characteristics. To give the reader a rough idea, a sensitive vertical range between approx. 50 to 85 km altitude and vertical resolutions between approx. 7 and 20 km have been reported in previous studies.

3.4.1 Data usage and related realization of the AVKs

The retrieval is based on profiles that are normalized with the a priori (Eq. 7), since the strong vmr gradient is numerically difficult to treat. This implies the existence of two realizations of the AVKs (Sect. 3.2; Eq. 8), $\mathbf{A}_{\text{frac}}$ and $\mathbf{A}_{\text{vmr}}$, which might lead to confusions, so that a comment on this in advance is in order.

The main application of the presented retrieved dataset is the comparison to modeled data or satellite observations with a focus on the temporal CO variability. These independent datasets have commonly a higher vertical resolution, so that they have to be convolved with the KIMRA AVKs (Eq. 6) to be directly comparable. For such kind of comparison, both realizations of the AVKs are equivalent as long as all quantities are consistently either normalized or not normalized. As will be shown in the following, the retrieval is optimized for normalized profiles and, in this case, the retrieval characteristics are more straightforward, so that the results might be easier to interpret if the normalized representation is used.

The retransformation to the vmr representation, reintroduces the strong gradient of CO, but also amplifies smaller retrieval artifacts (Sect. 3.4.5). The characteristics for this vmr representation are therefore not ideal. This is, however, only relevant if the vmr itself is of particular interest (in contrast to e.g. its variation in time) and individual KIMRA vmr profiles are regarded as stand-alone and not relative to each other or to independent data. Since such a stand-alone use is not a major application of the presented dataset, the presented KIMRA retrieval is not optimized for this case.

3.4.2 Sensitivity

The retrieved value at a certain target altitude is sensitive to the true profile if the area under the corresponding AVK is close to unity. Smaller areas indicate a greater influence of the a priori on the retrieved state. The area of the AVK for a certain altitude is calculated by summing up the respective row of the AVK matrix.

Physically, the lower limit of the sensitivity is in this case defined by the noise of the spectrum (since the spectrometer has a sufficient bandwidth, which could also be the limiting factor) preventing the broad and flat part of the line from being fitted uniquely. The upper limit is defined by the transition from the pressure broadening regime to the Doppler broadening regime (besides the influence of the frequency resolution of the spectrometer), in which the linewidth is mainly controlled by temperature and does not contain any altitude information anymore.

Assuming that an AVK area greater than 0.8 contains enough information from the measurement, we find general sensitivity (Fig. 4a) in a range of 34 to 87 km for the retrieval converted to vmr and a range of approx. 27 to 83 km for the fractional retrieval. This range matches the maximum expectations, but is narrowed by considering further criteria in the following.

Note that due to the comparatively high amount of CO in the thermosphere, the retrieval has some residual sensitivity up to 130 km, which has to be considered for the retrieval to be complete, but which is not sufficient to derive independent information.

3.4.3 Center of AVKs

The center of a certain AVK (weighted mean of all altitudes using the AVK entries as weighting factors) should ideally be located at the respective target altitude. Thus, the part of the center vs. target altitude relation that is close to the line of origin (Fig. 4b) indicates the altitude range where the retrieval works reasonably. The deviation from the line of origin has, however, to be seen in relation to the respective vertical resolution (Sect. 3.4.4). For this, the difference between corresponding center and target altitudes is shown normalized with the full width at half mean (FWHM) of the AVK in Fig. 4d.

This criterion is fulfilled for the fractional retrieval between 40 and 80 km, which defines the reasonable range of the retrieval in the normalized representation. The respective curve (Fig. 4b) for the vmr representation is, however, shifted to lower altitudes by about 4 to 10 km up to an altitude of about 70 km and even more so at higher altitudes. This behavior is the result of an amplification of negative overshoots of the vmr AVKs and will be discussed further in Sect. 3.4.5. The deviation from the line of origin has to be considered in data analyses using the vmr representation; the altitude of observed features does not directly correspond to the geometric altitude in the atmosphere anymore, but is shifted by a few kilometers to higher altitudes. This corresponds to 25 to 50 % of the FWHM between 40 and 60 km altitude (where the FWHM of the vmr represenation is meaningful; Sect. 3.4.4) and is therefore still below the order of the vertical resolution. Above 70 km, however, the center altitude does not further increase with the target altitude so that
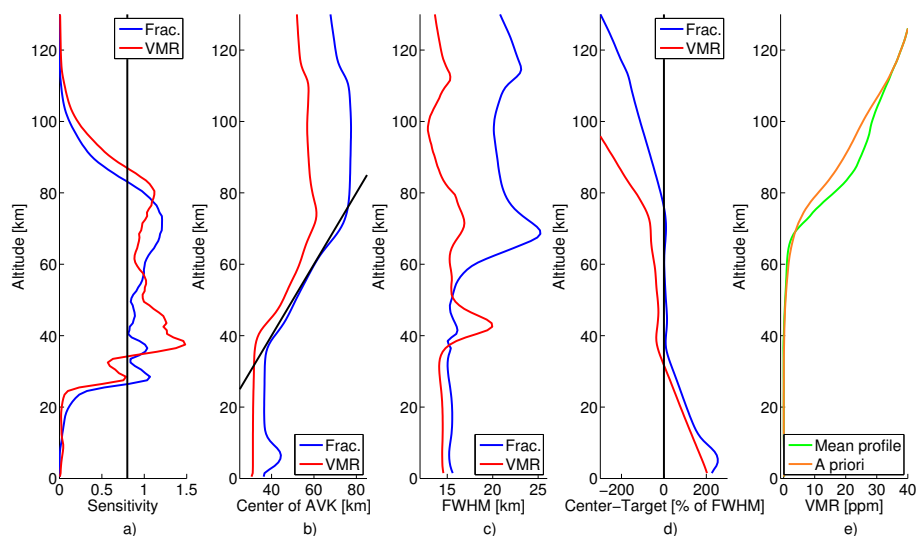
Fig. 4. Retrieval characteristics averaged over the complete dataset shown for the fractional retrieval (blue) and the retrieval converted to vmr (red). **(a)** Sensitivity given by the sum of the AVKs. The black solid line marks the threshold of 0.8, under which data is not considered to be reliable. **(b)** Altitude of the center of the AVKs. The black solid line marks the line of origin. **(c)** FWHM of the AVKs as a measure for the vertical resolution. Values for the vmr AVKs are not reasonable in all altitudes (Sect. 3.4.4). **(d)** The deviation of the curves in **(b)** from the line of origin normalized with the FWHM. **(e)** Mean profile of all retrieval results and the constant a priori.

the inclusion of this region in the vmr represenation should be considered with care.

This behavior is connected to special characteristics that the center vs. target altitude relation (Fig. 4b) generally exhibits also in the normalized representation, but which is there only relevant above 80 km altitude. First, the centers of the AVKs with target altitudes between 80 and about 110 km are constant at approx. 80 km. Second, above 110 km the centers of the AVKs even decrease again down to about 68 km (fractional retrieval). The latter is explained by the fact that the temperature in the thermosphere is increasing strongly, which leads to a stronger Doppler broadening. Accordingly, the Doppler broadened contribution to the line from 130 km has the same width as the pressure broadened contribution from about 68 km, so that a unique attribution to the altitude is impossible. However, this ambiguity is neglectable since the signal from above 110 km is generally low (Fig. 4a). In principle, this effect should also be present between 80 km and 110 km, but is superimposed by the limited frequency resolution of the spectrometer. The change of the linewidth with altitude in that region is small due to the cold temperatures around the mesopause and cannot be resolved anymore, so that all the contributions are attributed to a single altitude.

3.4.4 Vertical resolution

The vertical resolution of the measurement in a certain altitude is indicated by the FWHM of the respective AVK (Fig. 4c). For the fractional retrieval, we find a FWHM of about 16 km between altitudes of approx. 40 and 57 km, and

increasing values with an average of approx. 22 km between altitudes of 57 and 80 km. This suggests that the measurements provide two (and a fraction of a third) independent layers of information in the range of maximum sensitivity between 40 and 80 km. The FWHMs for the vmr AVKs $\mathbf{A}_{vmr}$ have to be treated with care, since some AVKs show an oscillating shape for which the FWHM-concept is not appropriate. Whereas the FWHM values of 15 to 20 km between 40 and 60 km altitude can be regarded as a good indication for the real vertical resolution, the values above are too low (Sect. 3.4.5).

An alternative measure for the degrees of freedom in the observation is the trace of the AVK matrix (Rodgers, 2000), which is 3.17 on average for the KIMRA CO retrieval. This matches the above values considering that there is some remaining information outside of the 40 to 80 km range. Furthermore, this measure of the degrees of freedom does not depend on the particular realization of the AVKs. Hence it is also valid for the vmr representation $\mathbf{A}_{vmr}$, suggesting independently from the FWHM concept, that the vertical resolutions of both representations are comparable.

Note that two maxima of the FWHM are found at approx. 70 km and 115 km respectively, which correspond to the ambiguity explained in Sect. 3.4.3.

It is emphasized here that the limited vertical resolution has to be taken into account for the use and interpretation of the data (e.g. comparisons to other datasets) by considering the appropriate realization of the AVKs using Eq. (6), depending on whether normalized quantities are used or not. The AVKs are therefore, together with the a priori, an essential part of the dataset.
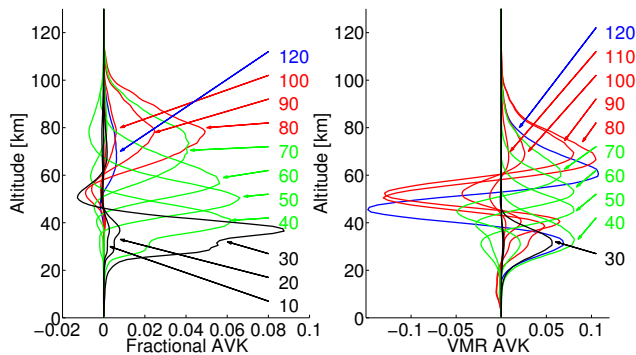
Fig. 5. Selected AVK functions for the measurement of 29 October 2009, 06:52 h, for several altitudes. Different colors represent vertical ranges with different measurement characteristics. The target altitudes in km of the respective kernels are imprinted with arrows. The 120 km kernel (blue) was multiplied by 50 to make it visible in the given scale. Left panel: fractional AVKs. The 110 km AVK has been omitted since it is to small. Right panel: vmr AVKs. The 10 and 20 km AVKs have been omitted for the same reason.
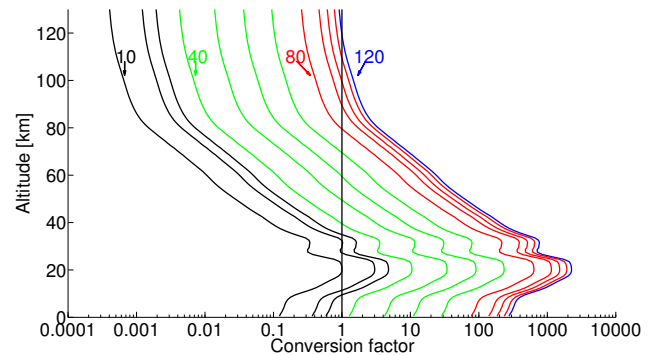
Fig. 6. Selected altitude-dependent factors for the conversion from fractional AVKs to vmr AVKs. Single curves, the labeling, and the coloring correspond to ones in Fig. 5, so that the curves belong to AVKs with target altitudes between 10 and 120 km in 10 km steps from left to right. It is obvious, that AVKs with high target altitudes are mainly amplified, whereas AVKs with low target altitudes are mainly diminished.

3.4.5 Individual AVK functions

Figure 5 shows a subset of both representations of AVKs related to the retrieval example discussed earlier (Sect. 3.3). In this subset all interesting altitude ranges are represented to illustrate the results of the preceding subsections (the fractional AVKs, Fig. 5 left panel, show these features more clear and are therefore discussed first):

- The range below the main sensitivity (below 40 km; black): the area of the AVKs increases with altitude, whereas all AVKs peak at the same altitude of approx. 37 km.

- The range of main sensitivity (between 40 and 80 km; green): the area of the AVKs is comparable and the AVKs peak at their respective target altitude, whereas the widths of the AVKs increase with altitude.

- The range above the main sensitivity where the spectrometer cannot resolve altitude information (between 80 and 110 km; red; see also Sect. 3.4.3): the area of the AVKs decreases with altitude, whereas all AVKs peak at about 80 km.

- The range above the main sensitivity where the spectrometer resolves ambiguity of the linewidths (above 110 km; blue; see also Sect. 3.4.3): the area of the AVKs is comparatively small. The peak altitude actually decreases with increasing target altitude.

The fractional AVKs of all altitudes have slight negative overshoots, which is common for such retrievals.

Figure 5 (right panel) shows the corresponding vmr AVKs $\mathbf{A}_{vmr}$, converted using Eq. (8). It is obvious that the negative overshoots are much more pronounced here, giving some of

the vmr AVKs an oscillatory shape. This is explained by the shape of the CO profile that goes into the conversion: The calculation of the pure conversion factors (evaluation of Eq. 8 with the matrix of ones in place of $\mathbf{A}_{frac}$; results shown in Fig. 6) reveals that, for each AVK, all entries below the target altitude are amplified whereas the entries above the target altitude are diminished. The result is that vmr AVKs with high target altitudes are strongly amplified by the conversion and formerly small negative overshoots become pronounced. This in turn affects the AVK diagnostics presented in Sects. 3.4.3 and 3.4.4. The entries below the target altitude gain more weight, which shifts the centers of the AVKs downward and due to the stronger oscillatory shape of some vmr AVKs, the FWHM-concept is partly not applicable anymore.

As a result, the overall appearance of the vmr AVKs does not look reasonable at first glance, which may cast doubts on the general retrieval performance, although the retrieval works adequately: First, the diagnostics related to the normalized retrieval result, $\mathbf{A}_{frac}$, are reasonable. Thus, particular data analyses and comparisons can be performed on the basis of normalized quantities, completely without consideration of the vmr AVKs. Second, looking closer at the vmr AVKs $\mathbf{A}_{vmr}$, it can be seen that the vmr AVKs in the range of 40 km to at least 70 km altitude are reasonable, although their center is shifted downwards by a few kilometers due to the stronger negative overshoot. Third, the impact of the pronounced oscillations of the vmr AVKs $\mathbf{A}_{vmr}$ with higher target altitudes is mostly weak. Considering a vmr AVK that has a second (negative) peak below the main peak of similar absolute strength, the meaning of such an AVK is that a change of 1 ppmv in the true atmosphere at either the one or the other peak altitude has a similar influence on the retrieved value. However, looking at the CO profile, a change

of 1 ppmv would be a much bigger relative change at the lower altitude in comparison to the higher altitude, and is much more unlikely.

3.5 Error assessment

3.5.1 Theory

The realization of the error assessment is based on the work done by Palm et al. (2010), and thereby also follows the description in Rodgers (2000). The deviation of the retrieved state $\hat{x}$ from the unknown true state x can be expressed as the sum of certain error contributions, in particular the smoothing error (Eq. 9), the forward model error (Eq. 10), the errors of the forward model parameters (Eq. 11), and the noise error (Eq. 12):

$$\hat{x} - x = (\mathbf{A} - \mathbf{I})\,(x - x_{\mathrm{a}}) \tag{9}$$
$$+ \mathbf{D}\,\Delta F\,(x,\,b,\,\hat{b}) \tag{10}$$
$$+ \mathbf{D}\,\mathbf{K}_{\mathrm{b}}\,(b - \hat{b}) \tag{11}$$
$$+ \mathbf{D}\epsilon \tag{12}$$

with b being the true forward model parameters, $\hat{b}$ the respective estimates used in the retrieval, $\mathbf{K}_{\mathrm{b}} = \frac{\partial F}{\partial b}$ the Jacobian of the forward model with respect to the parameters b, and ΔF the deviation of the forward model implementation from the true forward model.

The first two error sources are not examined here, since an estimate is difficult, and in this context not necessary. The smoothing error denotes that the retrieved profile is inexact due to the vertical averaging caused by the limited vertical resolution. For the estimation of this error, the true state, or at least a precise statistical description of the true state, is necessary (Rodgers, 2000). This description is not available, but since information about the vertical resolution is stored in the AVKs, another way of dealing with that error source is to provide the AVKs and the a priori together with the profiles, as it is done here. In comparisons, the smoothing error is automatically addressed by using Eq. (6). The other error not examined here is caused by possible deficiencies of the forward model, and can only be estimated using independent data or in comparison with other models. The performance of the forward model used in this study has already been examined by Melsheimer et al. (2005).

For the calculation of the third contribution, meaning the errors σ_{fp} caused by the uncertainties of the forward model parameters, the expression $\mathbf{D}\,\mathbf{K}_{\mathrm{b}}$ in Eq. (11) is identified as an AVK matrix with respect to these parameters, $\mathbf{A}_{\mathrm{b}}$, which is derived from the calculation of the respective derivatives

$$\mathbf{D}\,\mathbf{K}_{\mathrm{b}} = \mathbf{A}_{\mathrm{b}} = \frac{\partial \hat{x}}{\partial b}. \tag{13}$$

With an estimated covariance matrix of the forward model parameters $\mathbf{S}_{\mathrm{b}}$, the respective covariance matrix of the retrieved profile $\mathbf{S}_{\mathrm{fp}}$ is derived using

$$\mathbf{S}_{\mathrm{fp}} = \mathbf{A}_{\mathrm{b}}\,\mathbf{S}_{\mathrm{b}}\,\mathbf{A}_{\mathrm{b}}^{T}. \tag{14}$$

Finally, the standard deviation of the profile caused by the forward model parameters is given by

$$\sigma_{\mathrm{fp}}^{i} = \sqrt{S_{\mathrm{fp}}^{ii}}, \tag{15}$$

without consideration of off-diagonal entries.

The forth error contribution, caused by the noise on the spectrum σ_{η}, is calculated using the noise covariance matrix $\mathbf{S}_{\epsilon}$ via

$$\mathbf{S}_{\eta} = \mathbf{D}\,\mathbf{S}_{\epsilon}\,\mathbf{D}^{T} \tag{16}$$

and

$$\sigma_{\eta}^{i} = \sqrt{S_{\eta}^{ii}}. \tag{17}$$

3.5.2 Setup

The error contributions from five different forward model parameters have been considered. The first three (σ_{I_0}, $\sigma_{\gamma_{\mathrm{air}}}$, and $\sigma_{n_{\mathrm{air}}}$) belong to the main spectroscopic parameters, specifically the line intensity I_0, the pressure broadening parameter γ_{air} and its temperature dependency parameter n_{air} (see Bühler et al., 2005 and references therein for exact definitions). Furthermore, the contribution σ_T from the uncertainty of the used temperature profiles, as well as the contribution σ_{T_C} from a possible calibration error of the absolute spectrum, have been considered. The total error is given by

$$\sigma_{\mathrm{tot}}^{i} = \sqrt{\left(\sigma_{\gamma_{\mathrm{air}}}^{i}\right)^2 + \left(\sigma_{n_{\mathrm{air}}}^{i}\right)^2 + \left(\sigma_{I_0}^{i}\right)^2 + \left(\sigma_{T}^{i}\right)^2 + \left(\sigma_{T_C}^{i}\right)^2 + \left(\sigma_{\eta}^{i}\right)^2}. \tag{18}$$

The derivation of the underlying uncertainty values is explained in the following; the values are summarized in Table 2.

As for the spectroscopic parameters themselves, the HITRAN catalog is generally used also for estimates of the uncertainties. The uncertainty for the line intensity I_0 is given with a value lower than 1 %. However a comparison with the respective value in the JPL catalog (Pearson et al., 2010) shows a discrepancy of approx. 2 %, so this value is used instead. The other spectroscopic parameters are not covered by the JPL catalog.

For the error on the used SABER temperature profiles (Sect. 3.2), it is not enough to consider the given uncertainty for a single profile, since the effect of the locational mismatch of the satellite measurements has to be included. This can be addressed by taking the standard deviation of the averaged profiles in the collocation box into account. However, another complication comes from the fact that this box is filled only at the southern edge every 60 days (Sect. 3.2), which may introduce an additional systematic error. The maximum uncertainty that has to be expected from the temperature profiles has therefore been estimated by checking several configurations of collocated profiles (comparison of a complete box during the north-viewing mode phase with a subset of these profiles south of 52° N, a comparison of a

Table 2. Considered error contributions. See text for further justification.

Quantity	Used uncertainty	Reason	Reference
Line intensity I_0	2 %	Deviation of quantities in catalogs HITRAN and JPL	Rothman et al. (2005); Pearson et al. (2010)
Pressure broadening γ_{air}	2 %	Maximum error given in HITRAN	Rothman et al. (2005)
Temperature dependency n_{air}	5 %	Maximum error given in HITRAN	Rothman et al. (2005)
Temperature profile T below 80 km	5 %	Mismatch of measurement locations	
Temperature profile T above 100 km	10 %	Mismatch of measurement locations	
Temperature profile T in between	interpolated from 5 % to 10 %	Mismatch of measurement locations	
Calibration error	2 K	Conservative estimation including possible side effects	

north viewing mode phase (October 2009) with a real south-viewing mode phase (December 2009), as well as the standard deviations in these boxes). The individual tests showed uncertainties of a similar order of magnitude and a rough estimation of the maximum values has been derived from these values.

A conservative estimate of the calibration error of the absolute spectrum is in the order of 2 K. The tolerance of the adjustable reference load is about one order of magnitude lower, but in the sense of a rough estimation of the maximum uncertainty side effects, as e.g. a possible temperature drift, were included in this larger error.

3.5.3 Results of the error estimation

The single contributions to the total error may differ from spectrum to spectrum, which is expected because of the varying signal-to-noise ratio (Sect. 2.3). However, the following general statements can be made (examples are shown in Fig. 7):

– According to the shape of the CO profile, the absolute error increases strongly with altitude, and is approx. 0.1 ppmv at 50 km and approx. 3 ppmv at 80 km altitude.

– The dominating contributions to the total uncertainty σ_{tot} are the noise error σ_η and the temperature error σ_T.

– Frequently, the spectroscopic contribution σ_{I_0} shows a peak of a few tenths of a ppmv at approx. 60 km, which is strong enough to dominate the total uncertainty σ_{tot} in this altitude (Fig. 7, bottom panel).

– The other spectroscopic contributions as well as the calibration error are negligible.

– The error σ_{I_0} is systematic and also σ_T may have a systematic nature, since it can be caused by a southward bias of the collocated SABER temperature profiles. This means that a reduction of the total error σ_{tot} by averaging over a subset of KIMRA profiles can only be achieved as long as the noise error σ_η dominates. In this sense, these systematic contributions define the
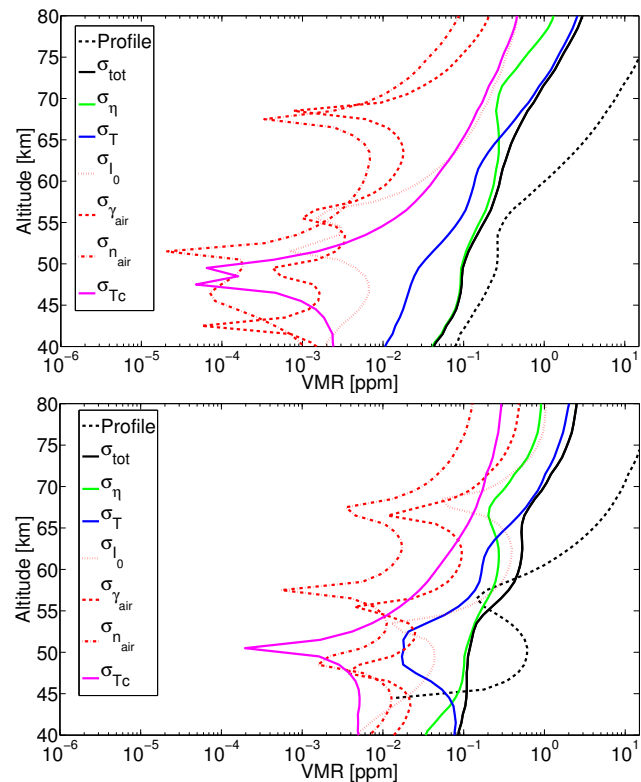

Fig. 7. Typical examples of error contributions. The dominating contributions to the total error σ_{tot} come from the measurement noise error σ_η, from the temperature error σ_T, and frequently from the spectroscopic error σ_{I_0}. For comparison, the corresponding vmr profiles are also included (black dashed lines). Top panel: example of 29 October 2009, which has no dominating spectroscopic contribution. Bottom panel: example of 4 February 2009, which shows a pronounced spectroscopic contribution at approx. 60 km.

lower limit of the total error which can be achieved by averaging of KIMRA profiles.

3.5.4 Variation of the a priori

In addition to the error analysis based on the standard retrieval theory, an experiment with different CO a priori

Table 3. Details of the a priori influence experiment, valid for the vertical range of the main sensitivity between 40 and 80 km altitude.

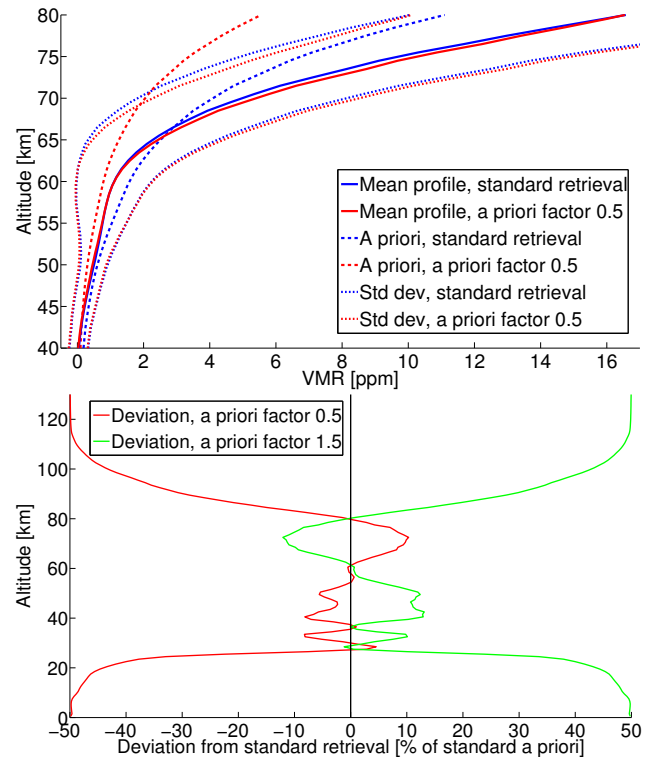| Modification of a priori	+50 %	−50 %
Min. deviation	−12 %	-8 %
Max. deviation	+13 %	+10 %
Mean abs. deviation	8 %	4 %
Mean deviation	1 %	1 %
Partial col. deviation	4 %	−0.3 %

Fig. 8. Test of the retrieval stability when the a priori is changed by a factor of 0.5 or 1.5 respectively. Top panel: mean profiles, associated standard deviations, as well as a priori profiles for the standard retrieval and one modified retrieval setup (factor 0.5) in the range of sensitivity between 40 and 80 km. It is obvious, that the change of the mean profile introduced by an a priori change is much smaller than the standard deviation, which is mainly produced by the annual variability. Profiles of the factor 1.5 case behave similarly and are not shown. Bottom: deviation of the mean profiles of both modified cases from the standard retrieval profile, plotted for the complete vertical range, normalized with the standard a priori. The deviation is small in the range of sensitivity between 40 and 80 km and approaches, as expected, 50 % where the sensitivity vanishes completely.

profiles was carried out, to investigate the influence of the a priori on the retrieval result independently from the AVK discussion (Sect. 3.4). For that the standard a priori (Sect. 3.2) was reduced (alternatively raised) by 50 % constantly over the full altitude range, whereas the a priori covariance in absolute units was kept constant. The complete dataset was retrieved with this modified setup. To find systematic effects, total average profiles over the three different datasets were calculated (Fig. 8, top panel) as well as the deviations to the standard results (Fig. 8, bottom panel). In addition the partial columns of CO between 40 and 80 km were compared.

The results from the modified setups slightly oscillate around the standard profile in the range of the main sensitivity, whereas the deviation aside of the main sensitivity approaches the original magnitude of 50 %, as expected. In conclusion, an incorrect choice of the a priori may introduce a systematic bias of about 6 % on average (for details see Table 3) in the range of main sensitivity on the basis of a 50 % deviation of the a priori.

4 Retrieved CO time series

The retrieved time series of CO profiles will be described here only briefly, since its detailed scientific application is beyond the scope of this paper and will be published separately. It is more illustrative to present the measured time series on the retrieval grid with narrow grid spacing although the real vertical resolution is coarser (Sect. 3.4). Therefore, the reader is reminded, that altitude levels close together are not independent of each other, i.e. the AVKs have to be considered in quantitative analyses.

Several well-known dynamical features such as the polar winter descent, sudden stratospheric warmings (SSWs), and final warmings are identified in the KIMRA CO time series (Fig. 9). The descent of mesospheric air is obvious in fall 2009: The location of the strong vertical gradient is shifted downward by approx. 20 km (e.g. 75 to 55 km for the 4 ppmv level) from mid September to mid November. Therefore the estimated average descent velocity is roughly 300 m d^{-1}, which is in general agreement with previous studies (e.g. Funke et al., 2009; Forkman et al., 2005; Allen et al., 2000).

As the nature of a SSW is a strong perturbation of the polar winter circulation, CO in the polar vortex is also affected. In particular, the CO vmr shows a fast decrease during a SSW (Manney et al., 2009). A SSW may be followed by a strong downwelling of air masses, which in turn increases the CO rapidly. The presented CO time series contains the two SSWs that occurred during the measurement period in January 2009 and January 2010 respectively.

The breakup or final warming of the vortex is the beginning of the transition from the winter to the summer circulation. It leads like a sudden stratospheric (midwinter) warming to a decrease in the CO vmr. Major interest has been in the timing of the breakup, which is very variable with a possible timespan from February to May (Waugh and Rong, 2002) and which influences the spring polar temperature and ozone
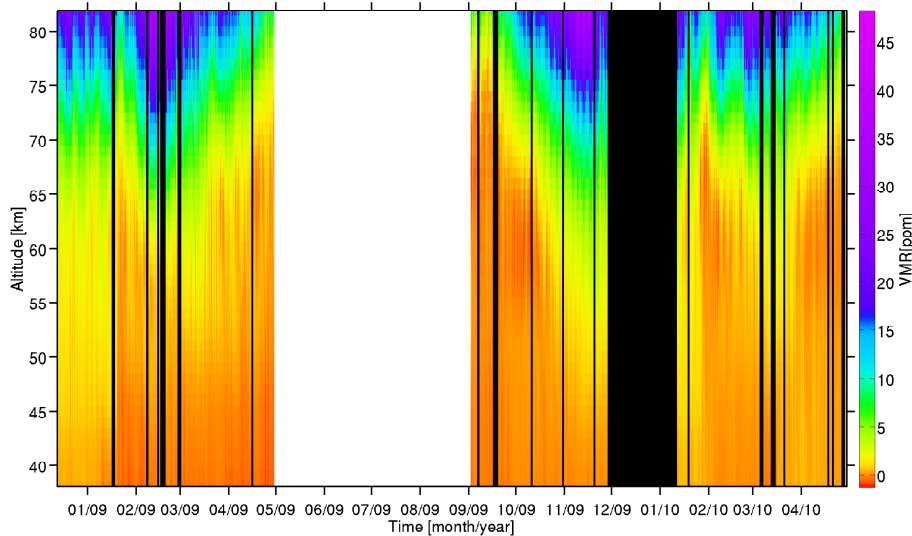
Fig. 9. Time series of the retrieved CO profiles covering the complete analyzed period. The descent of air in fall 2009, the two sudden stratospheric warmings in 2009 and 2010, respectively, as well as the two final warmings in both winters can be easily identified. The black areas mark periods without measurements due to rainy weather or maintenance of the instrument. The white area marks the summer period from which CO measurements can generally not be retrieved reasonably.
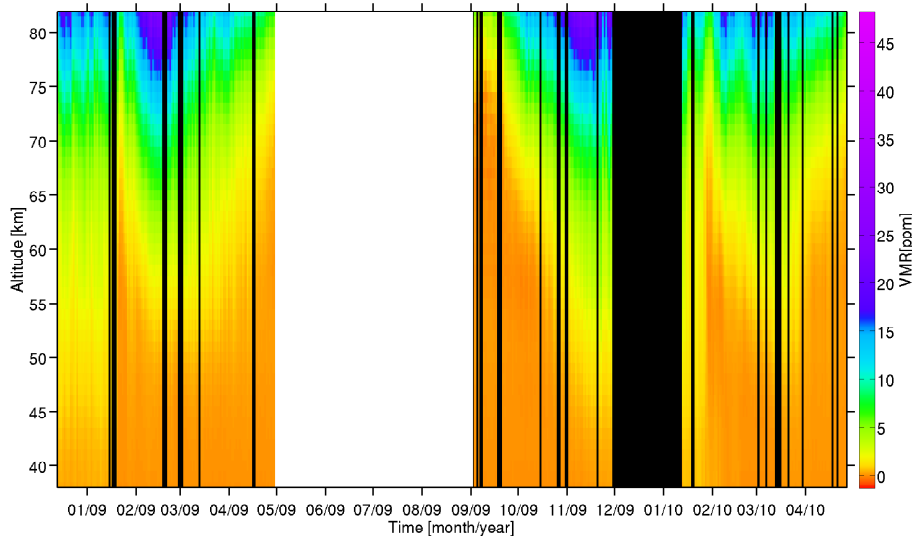

Fig. 10. Time series corresponding to Fig. 9, but measured by the MLS satellite instrument, showing that all major features are contained similarly in both datasets. Collocated profiles within a distance of 500 km around Kiruna were selected, convolved with the KIMRA AVK and averaged daily.

(Waugh et al., 1999). The presented time series (Fig. 9) of CO profiles contains the breakup phases during spring 2009 and spring 2010.

To allow for a qualitative consistency check between independent measurements, the corresponding time series of the satellite instrument MLS is shown in Fig. 10. A detailed satellite comparison of average profiles, including an instrument description, is presented in Sect. 5. Here the main intention is to show that all the major features described above are consistently measured by both instruments. Furthermore, the KIMRA dataset shows more variability on short timescales, whereas the MLS time series looks smoother. This comes from the averaging that has to be applied to the collocated MLS profiles; all MLS profiles within a distance of 500 km around Kiruna were selected, convolved with the KIMRA AVK functions using Eq. (6) and then averaged daily.

5 Satellite comparison

One important application of ground-based observations is the intercomparison with satellite data to investigate the agreement between these independent methods in certain regions. However, to our knowledge there are no such comparisons published for strato-mesospheric CO in polar regions and using the microwave technique. Data of one ground-based microwave radiometer in the mid-latitudes was included in the validation of the ACE-FTS CO product, but here only two coincidences were found (Clerbaux et al., 2008). Indeed, properties of both the polar region and the microwave technique cause special difficulties in the comparison of polar CO:

– The CO vmr in this region shows strong horizontal and vertical gradients, so that the choice of tight collocation criteria is particularly important.

– The polar coverage of some satellite instruments is sparse, especially during polar night, which demands, in contrast to the first point, for relaxed collocation criteria.

– Although the upper limit of reasonable information of the KIMRA measurements is approx. 80 km, there is some residual sensitivity up to approx. 130 km (Sect. 3.4.2), where also the available satellite datasets cannot provide reasonable information anymore. Due to the limited vertical resolution of the KIMRA measurements (considered by smoothing with the KIMRA AVKs), however, the profile parts of this region may also affect the comparison in the range of interest below 80 km.

Nevertheless, we relate here our dataset to those of three recent satellite instruments using different measurement techniques. Although being not the main motivation, another outcome of this study is a rough comparison of the satellite instruments with each other. Therefore it is an addition to the satellite intercomparisons included in the extensive validation studies (e.g. Pumphrey et al., 2007; Clerbaux et al., 2008) in the sense, that this comparison is focused spatially on a certain area around Kiruna. However, it is also restricted to the coarse vertical resolution of the KIMRA instrument, so that smaller vertical structures cannot be compared.

Note that this satellite comparison is restricted to the comparison of mean profiles. Whereas a detailed comparison of the time evolution will be conducted in future, the general consistency of the datasets measured by KIMRA and the satellite instrument MLS was already shown in Sect. 4.

5.1 Procedure

The analysis of systematic deviations between the datasets is based on mean profiles of all datasets for the analyzed KIMRA period. The procedure with which these profiles are derived is described here briefly. First, the original satellite profiles are sorted according to following collocation criteria:

– Area: circle around Kiruna with the radius R.

– Deviation of potential vorticity (PV): PV is used to separate inner-vortex air from mid-latitudinal air, in which the CO vmr is much lower during polar winter. The PV is calculated from ECMWF Operational Analysis wind fields in 40, 50 and 60 km altitude. The deviation

$$\Delta PV(z) = \frac{PV_{Kiruna}(z) - PV_{Sat}(z)}{PV_{Kiruna}(z)} \quad (19)$$

may not exceed a certain threshold in any of the altitudes for the profile to be considered.

– Period: profiles have to be measured at the same day to be considered comparable throughout this study.

The profiles selected are interpolated to the KIMRA retrieval grid, on which the analysis is performed.

As explained above, information from the unreasonable parts of the satellite profiles may affect the comparison in the interesting vertical range. To avoid that physically implausible values are considered, the upper parts of the satellite profiles are replaced with the KIMRA a priori before the convolution with the KIMRA AVKs. This in turn may artificially improve the mutual agreement between the satellite datasets in the upper part, so that the considered altitude range has still to be restricted, after the convolution with the AVKs, to a lower top altitude than it would nominally be possible (Table 4). The modified satellite profiles are convolved with the respective KIMRA AVK functions (Eq. 6) using the vmr AVK functions $\mathbf{A}_{vmr}$ of the closest KIMRA measurement for each satellite profile. Note that we use here intentionally the vmr representation of the dataset over the widest possible altitude range between 40 and 80 km, to investigate also the behavior between 70 and 80 km altitude, the region in which the vmr representation has to be treated with care (Sect. 3.4).

The next step, in which daily averages from the convolved profiles are computed, results in a time series of one profile per day and dataset, in which single datasets may still have gaps due to the collocation criteria or lack of measurements. Such periods with a gap in at least one of the datasets will be removed in all other datasets. Thus the resulting time series contains only days with at least one measurement in every single dataset, which minimizes a possible bias due to different periods in the average. The averages have been computed as weighted averages with the inverse standard deviation of each original profile as weighting factor.

In the last step, these preprocessed time series are averaged to produce the mean profiles for the comparison x_{Sat} and x_{KIMRA} respectively. Besides these profiles themselves, also the deviation

$$\Delta x = x_{Sat} - x_{KIMRA} \quad (20)$$

Table 4. Properties of the satellite instruments considered in this study.

Dataset	Technique	Version	Nominal limit [km]	Used limit [km]	Number of profiles	Reference
Aura-MLS	microwave, limb	3.3	≈ 85	70	24 682	Pumphrey et al. (2007), Livesey et al. (2011)
ACE-FTS	infrared, solar occulatation	3.0	≈ 95	80	168	Clerbaux et al. (2008)
MIPAS NOM	infrared, limb	V4O_CO_200 (IMK/IAA)	≈ 70	60	2451	Funke et al. (2009)
MIPAS MA	infrared, limb	V4O_CO_501 (IMK/IAA)	≈ 95	80	72	

is evaluated. Note that we found a possible normalization of this deviation with the KIMRA profile x_{KIMRA} not to be insightful, since the strong gradient of the CO profile, as well as profile values close to zero (Sect. 3.3), produce large values, thus a bumpy curve which, is difficult to interpret.

5.2 Satellite instruments

Three recent satellite instruments, MLS, ACE-FTS and MIPAS, are considered in this comparison (see Table 4 for basic properties).

MLS (Microwave Limb Sounder) flies on the Aura satellite in a sun synchronous polar orbit and measures microwave emission in limb viewing geometry (Waters et al., 2006). The dataset provides by far the largest numbers of possible coincidences, so that first, the tightest collocation criteria are applied for MLS and second, the influence of relaxing these criteria is studied using MLS. However, the reasonable vertical range after the AVK convolution (upper limit 70 km) does not cover the full KIMRA range (Sect. 5.1) .

ACE-FTS (Atmospheric Chemistry Experiment – Fourier Transform Spectrometer) is an infrared Fourier transform spectrometer, measuring atmospheric absorption in solar occultation mode (Clerbaux et al., 2008). This technique produces high quality profiles, but only a small number of possible coincidences, so that relaxed collocation criteria have to be used. Nevertheless, the ACE-FTS comparison is interesting because of the good vertical coverage, which includes the full KIMRA range also after the convolution with the KIMRA AVKs.

MIPAS (Michelson Interferometer for Passive Atmospheric Sounding) onboard the Envisat satellite also is a Fourier transform spectrometer but measures atmospheric infrared emission in limb viewing geometry. Measurements are performed in three different modes covering different vertical ranges. CO data of the nominal mode (NOM) and the middle atmosphere mode (MA, observations every 10th day) are available for this study. The NOM dataset provides more possible collocations but allows only reasonable

comparisons up to 60 km whereas the MA mode provides, like ACE-FTS, a limited number of collocations with full vertical coverage. MIPAS CO data versions used in this study (V4O_CO_200 and V4O_CO_501 for NOM and MA observations, respectively, generated by IMK/IAA) are based on version V3O_CO_9+10 (Funke et al., 2009) with some minor modifications related to the changed spectral resolution since 2005.

5.3 Comparison with MLS

The dense MLS dataset allows for the tightest collocation criteria in this study ($R = 50$ km, $\Delta PV = 5\,\%$) for which 29 days with coincidences are found (Fig. 11 red dashed curve; see Table 5 for an overview of all experiments). The deviation between KIMRA and MLS is in the range of -0.2 and 0.2 ppmv between 40 and 65 km, which is in the same order of magnitude as the estimated systematic error contributions for the KIMRA dataset (Sect. 3.5.3). Above 65 km the deviation shows an increasing high bias for KIMRA with a maximum deviation of -2.5 ppmv at 70 km which exceeds the estimation of 1 ppmv.

Looking at the shape of the deviation, it is obvious, that it oscillates around zero between 40 and 65 km, representing a systematic difference of the profile shapes of KIMRA and MLS: The MLS profile is more curved, whereas the KIMRA profile shows a weaker increase of CO with altitude up to about 60 km and a stronger increase above, which then results in the large deviation at 70 km. This difference of the profile shapes can be recognized more or less pronounced in all comparisons in the following.

5.3.1 Influence of collocation criteria

Figure 11 also shows averages of MLS profiles in different areas around Kiruna. First, no PV criterion was applied, whereas second only profiles in the respective area with $\Delta PV < 5\,\%$ were selected.
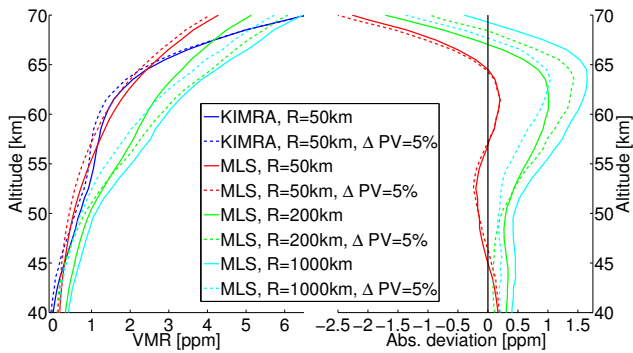
Fig. 11. Investigation of the influence of the collocation area using the MLS dataset. In the first case (solid lines) only the area criterion with different radii R was applied. In the second case (dashed lines) a PV threshold of $\Delta PV = 5\%$ was additionally applied. Left panel: mean profiles derived according to Sect. 5.1. KIMRA profiles are only shown for the tightest collocation criteria since their sensitivity to a criterion change is low (a dependency only exists, if the averaged period changes as result of a criterion change). Right panel: deviation between the KIMRA and the satellite profiles calculated with Eq. (20).

For all cases, the difference of the profile shape with respect to the KIMRA profile remains, but instead of being centered around zero, the oscillatory part of the deviation is shifted into the positive sector, which means that the MLS profiles show an increasing high bias up to 69 km altitude with an increasing collocation area. This behavior is expected, since CO increases non-linearly toward the winter pole, so that a widening of the collocation area in meridional direction automatically leads to an increasing average value. If, in addition, the allowed PV deviation is restricted, this relation is not clearly identified anymore; e.g. the agreement is better for $R = 1000$ km and $\Delta PV < 5\%$ than for $R = 200$ km and $\Delta PV < 5\%$. The reason for this might be an effect of the lower number of coincidences when the PV criterion is applied, although the comparatively dense MLS dataset was used here.

Figure 12 shows the resulting profiles and deviations of a similar experiment, in which the ΔPV threshold was varied in the maximum area with $R = 1000$ km. Again, the deviation of the profile shape is similar and the high bias for MLS is increased by relaxing the ΔPV threshold. However, with a PV threshold of greater than 10 % only a small number of profiles in the collocation area are rejected. Thus, the results obtained for different values of ΔPV greater than or equal to 10 % do not differ much, whereas the 5 % threshold reduces the deviation between KIMRA and MLS. This underlines the importance of keeping this limit in the order of 5 % or lower, which was, however, only possible for the MLS dataset.
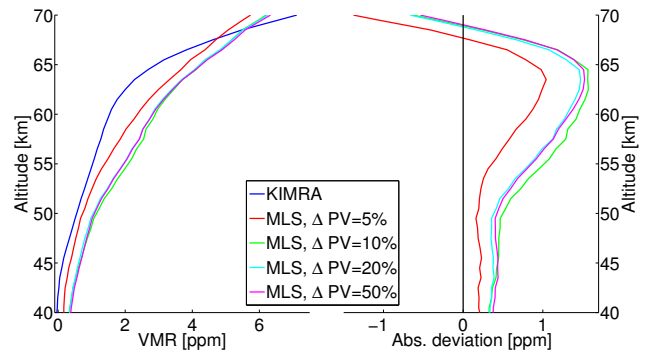

Fig. 12. Investigation of the influence of the PV collocation criterion using the MLS dataset in a constant radius of $R = 1000$ km. Left panel: mean profiles derived according to Sect. 5.1. Right panel: deviation between the KIMRA and the satellite profiles calculated with Eq. (20).

5.3.2 Influence of measurement period

This experiment was performed to clarify, if the observed deviation of the profile shape depends on the observation period, i.e. on the amount of CO during the measurements. In addition to the collocation criteria $R = 200$ km and $\Delta PV = 5\%$, five periods were chosen, for which average profiles were calculated: two periods of high CO after the fall descent in both winters, as well as three periods with low CO after the final warmings in both winters and the SSW 2010.

Although the number of coincidences for the single cases are small, the shape deviation is by tendency common to all periods (Fig. 13, only two selected cases are shown). But additionally, the experiment indicates that the oscillatory pattern is vertically shifted between high and low CO periods. This can be seen by looking at the individual maximum of the deviation, which is below 60 km for the high CO cases and above approx. 64 km for the low CO cases. This behavior appears plausible since the high CO scenarios are produced by a downward transport of CO, which roughly also shifts the CO profile and its properties to lower altitudes.
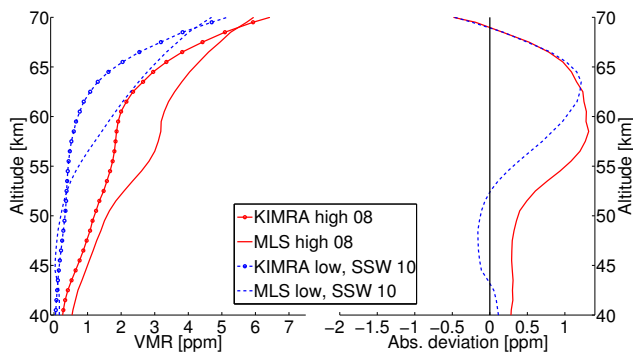
5.4 Multi-instrument comparison

The extension of the comparison to the other satellite datasets is difficult, since relaxed collocation criteria have to be chosen (Table 5), contradicting the findings made with the MLS collocation experiments. Furthermore, despite this relaxation the number of days with coincidences still remains low, so that effects of the small sample size cannot be excluded.
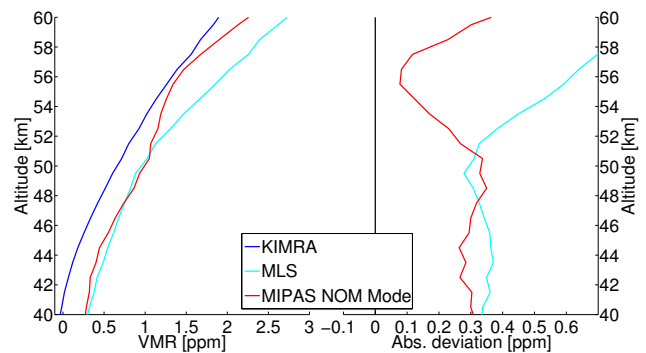
After MLS, the MIPAS NOM dataset provides the most collocations with moderate collocation criteria, however, the comparison is restricted to 40 to 60 km altitude (Fig. 14). Between 40 and 50 km the MIPAS NOM and the MLS profile are in close agreement, showing a 0.3 ppmv high bias in comparison to KIMRA, which corresponds to the widened collocation criteria (Sect. 5.3.1). Between 50 and 55 km MIPAS

Table 5. Summary of setups of the satellite comparison experiments.

Experiment	R [km]	ΔPV [%]	Period	Days	Figure
Area (MLS)					Fig. 11
	50		complete	40	
	200		complete	215	
	1000		complete	300	
	50	5	complete	29	
	200	5	complete	101	
	1000	5	complete	157	
PV (MLS)					Fig. 12
	1000	5	complete	157	
	1000	10	complete	270	
	1000	20	complete	293	
	1000	50	complete	300	
Period (MLS)					Fig. 13
High CO 2008	200	5	15 Dec 2008–15 Jan 2009	6	
High CO 2009	200	5	1 Nov 2009–30 Nov 2009	9	
Low CO 2009	200	5	1 Apr 2009–30 Apr 2009	14	
Low CO 2010 (SSW)	200	5	29 Jan 2010–28 Feb 2010	7	
Low CO 2010	200	5	1 Apr 2010–30 Apr 2010	9	
Multi Instrument					
MIPAS NOM, MLS	250	20	complete	42	Fig. 14
ACE-FTS, MLS	1000	20	complete	22	Fig. 15
MIPAS MA, MLS	1000	20	Jan 2009–Apr 2009	9	Fig. 16
ACE, MIPAS MA, MLS	1000	50	18 Mar 2009	1	Fig. 17

Fig. 13. Investigation of the influence of the averaged period using the MLS dataset in a constant radius of $R = 200$ km. Two cases with comparatively high (red) or low (blue) CO values are shown. Three more cases were analyzed but are not shown for clarity of the figure; for details see Table 5. Left panel: mean profiles derived according to Sect. 5.1. Right panel: deviation between the KIMRA and the satellite profiles calculated with Eq. (20).

Fig. 14. Comparison of KIMRA with MIPAS (NOM mode) and MLS using the collocation criteria $R = 250$ km and ΔPV $= 20$ %. 42 days with coincidences were found. Left panel: mean profiles derived according to Sect. 5.1. Right panel: deviation between the KIMRA and the satellite profiles calculated with Eq. (20).

NOM approaches the KIMRA profile with a minimum deviation of less than 0.1 ppmv whereas the deviation of MLS and KIMRA gets stronger in accordance with the systematic deviation of the profile shape. Above 55 km also MIPAS shows this tendency of an increasing deviation. This, together with the shown comparisons including ACE-FTS and MIPAS MA

that cover the complete KIMRA altitude range (Figs. 15, 16, and 17), exemplifies the following findings which are common to all multi-instrument satellite comparisons performed:

– In tendency, the profile shape of the KIMRA dataset deviates similarly from all satellite datasets as described in Sect. 5.3.
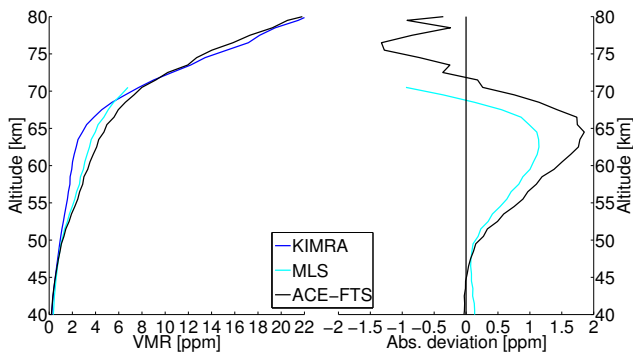
Fig. 15. Comparison of KIMRA with ACE-FTS and MLS using the collocation criteria $R = 1000$ km and $\Delta PV = 20$ %. 22 days with coincidences were found. Left panel: mean profiles derived according to Sect. 5.1. Right panel: deviation between the KIMRA and the satellite profiles calculated with Eq. (20).

Fig. 16. Comparison of KIMRA with MIPAS (MA mode) and MLS using the collocation criteria $R = 1000$ km and $\Delta PV = 20$ %. 9 days with coincidences were found. Left panel: mean profiles derived according to Sect. 5.1. Right panel: deviation between the KIMRA and the satellite profiles calculated with Eq. (20).

- The satellite datasets mostly show a high bias in comparison with the KIMRA dataset below 65 km, which is in the order of the high bias caused by relaxed collocation criteria (Sect. 5.3.1). Thus, this bias is not necessarily an intrinsic property of the KIMRA dataset.

- In many cases, the satellite profiles deviate among each other in the same order of magnitude as they deviate from the KIMRA profile. The reason for this is probably a mixture of three error sources. First, there are known systematic deviations between the single satellite datasets (e.g. ACE-FTS and MIPAS ±26 % in all altitudes and ACE-FTS and MLS −25 % to −100 % between 42 to 65 km; see Clerbaux et al., 2008 for details and definitions), however these are usually estimated using global data and may differ for a comparison restricted to polar latitudes. Second, the wide collocation criteria may also lead to biases between the satellite datasets and third, noise effects play a role due to the small number of coincidences.

5.5 Discussion of the profile shape deviation

The reasons for the deviation of the KIMRA profiles in comparison to the satellite profiles are speculative, but it is likely that the general error source has to be sought in the KIMRA measurements, since the deviation appears consistently in the comparisons to all the satellite datasets. Note that similar structures were previously found for O_3 in ground-based microwave vs. satellite comparisons by Boyd et al. (2007) and Palm et al. (2010), who also attribute the reason to the ground-based microwave measurements. Figure 7, bottom panel, suggests, that oscillatory systematic deviations may arise from uncertainties in the spectroscopic parameters, however, this can also be a result of a complex interplay of many instrumental and retrieval parameters.
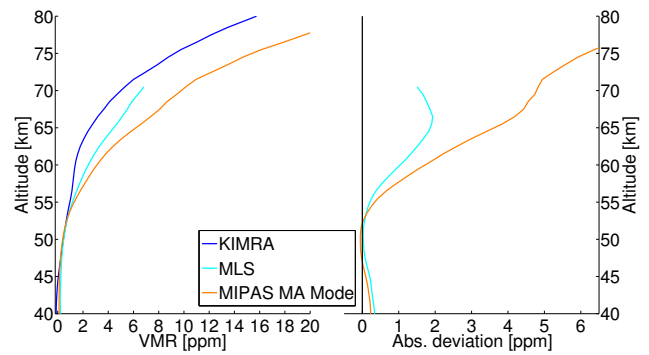
Generally the error source of different vertical resolutions is excluded by the convolution of all datasets with the KIMRA AVKs. This in turn means, that the established deviation is also smoothed by the AVKs and does not directly correspond to real atmospheric altitudes. Having in mind, that the KIMRA vertical resolution is about 22 km at 80 km altitude, the strong high bias for KIMRA in this region indicates a general discrepancy in the region between 70 and 90 km, where satellite observations also get more uncertain.

6 Conclusions

This work presents ground-based CO measurements of the Kiruna microwave radiometer KIMRA, located in northern Sweden (67.8° N, 20.4° E).

The instrument measures the CO emission line at 230 GHz together with O_3 continuously from September to April during each winter. Here, we have analyzed the CO spectra of the two winters, 2008/2009 and 2009/2010. This dataset includes approx. 1500 spectra with a mean integration time of approx. 1 h.

Vertical profiles of the CO vmr have been retrieved using the optimal estimation approach according to Rodgers (2000). The a priori profile as well as the a priori covariance matrix needed for this approach have been kept constant for the complete period, so that the variations with time of the retrieved profiles come certainly from the measurements.

A detailed analysis of the averaging kernel (AVK) functions has revealed that the measurements are sensitive between 40 and 80 km altitude with a vertical resolution of 16 to 22 km. Thus the obtained profiles are smoothed due to the limited vertical resolution, which has to be considered in comparisons by convolving better resolved profiles with the KIMRA AVKs. Furthermore, the AVKs show contributions in the received signal from up to 130 km altitude, which
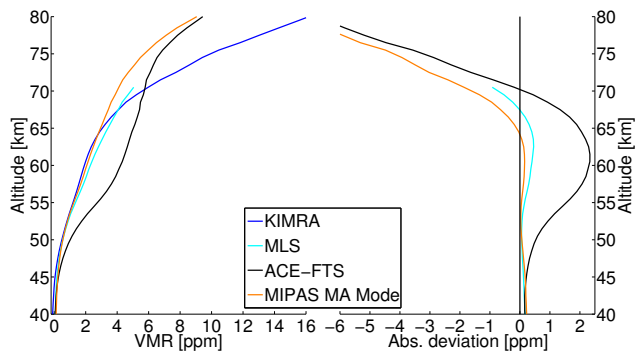
Fig. 17. Comparison of KIMRA with ACE-FTS, MIPAS (MA mode), and MLS using the collocation criteria $R = 1000$ km and ΔPV $= 50$ %. 1 day with coincidences was found. Left panel: mean profiles derived according to Sect. 5.1. Right panel: deviation between the KIMRA and the satellite profiles calculated with Eq. (20).

comes from the special shape of the CO vmr profile that is steeply increasing toward the thermosphere.

An error assessment has been performed to estimate potential errors of the retrieved profiles arising from different sources in the measurement and retrieval process. We have found that the total error increases with altitude from approx. 0.1 ppmv at 50 km altitude to approx. 3 ppmv at 80 km altitude. The main contributions to the total error arise from the noise on the spectra and the uncertainty of the used temperature profiles. Frequently, the error at about 60 km altitude is dominated by the uncertainty of the line intensity used for the forward model calculation.

The KIMRA dataset has been used in this work for a detailed comparison with CO data from recent satellite instruments. Included in this comparison are the instruments MLS on Aura, ACE-FTS, and MIPAS on Envisat (nominal mode and middle atmosphere mode). To our knowledge, a comparison of ground-based microwave observations and satellite measurements of strato-mesospheric CO has not been published in such detail before.

MLS, which provides the most dense dataset, has been used to investigate the influence of the collocation criteria first. Whereas no bias has been found below 65 km altitude between KIMRA and MLS for a maximum allowed distance of 50 km, a high bias for MLS was introduced by widening this distance, which is expected because of the horizontal CO distribution above the winter pole. The experiment additionally suggests, that the PV difference of profiles, which are considered as collocated, should not be greater than 5 %.

The comparison including also the other instruments has generally been complicated by the small number of coincidences, even if the collocation criteria are strongly relaxed in contrast to the previous findings. Although noise effects and sampling errors can therefore not be excluded, the comparison suggests that there is general agreement between KIMRA and the satellites instruments below 65 km altitude,

but a high bias for KIMRA above 65 km, which increases with altitude and reaches the order of 5 ppmv at 80 km altitude. Furthermore, the shape of the KIMRA profile appears to be systematically different from the satellite profiles: the satellite profiles are more curved, whereas the KIMRA profile shows a weaker increase of CO with altitude up to about 60 km altitude and a stronger increase above. The reason for this deviation is not clear, but it seems to be connected with the ground-based microwave measurements.

It has been shown qualitatively that the retrieved time series of CO profiles contains all the expected dynamical features of the polar winter middle atmosphere, the descent of mesospheric air in fall 2009, the sudden stratospheric warmings in 2009 and 2010, as well as the final warmings in both years. A quantitative analysis of these features is, however, beyond the scope of the present paper and will be carried out later.

References

Aellig, C. P., Kämpfer, N., and Hauchecorne, A.: Variability of mesospheric CO in the fall and winter as observed with ground-based microwave radiometry at 115 GHz, J. Geophys. Res., 100, 14125–14130, 1995.

Allen, D., Stanford, J., Nakamura, N., López-Valverde, M., López-Puertas, M., Taylor, F., and Remedios, J.: Antarctic polar descent and planetary wave activity observed in ISAMS CO from April to July 1992, Geophys. Res. Lett., 27, 665–668, 2000.

Anderson, G. P., Clough, S. A., Kneizys, F. X., Chetwynd, J. H., and Shettle, E. P.: AFGL atmospheric constituent profiles (0–120 km), Tech. Rep. TR-86-0110, AFGL, 1986.

Berg, H., Krupa, R., Hochschild, G., Kopp, G., and Kuntz, M.: Millimeter wave radiometer with adjustable internal calibration load for high resolution measurements of stratospheric constituents, in: Proceedings of 2nd ESA Workshop on Millimetre Wave Technology and Applications: Antennas, Circuits and Systems, 372–377, 1998.

Bevilacqua, R. M., Stark, A. A., and Schwartz, P. R.: The Variability of Carbon Monoxide in the Terrestrial Mesosphere as Determined From Ground-Based Observations of the $J = 1 \rightarrow 0$ Emission Line, J. Geophys. Res., 90, 5777–5782, 1985.

Borsdorff, T. and Sussmann, R.: On seasonality of stratomesospheric CO above midlatitudes: New insight from solar FTIR spectrometry at Zugspitze and Garmisch, Geophys. Res. Lett., 36, L21804, doi:10.1029/2009GL040056, 2009.

Boyd, I. S., Parrish, A. D., Froidevaux, L., von Clarmann, T., Kyrölä, E., Russell, J. M., and Zawodny, J. M.: Ground-based microwave ozone radiometer measurements compared with Aura-MLS v2.2 and other instruments at two Network for Detection of Atmospheric Composition Change sites, J. Geophys. Res., 112, D24S33, doi:10.1029/2007JD008720, 2007.

Bühler, S., Eriksson, P., Kuhn, T., von Engeln, A., and Verdes, C.: ARTS, the atmospheric radiative transfer simulator, J. Quant. Spectrosc. Ra., 91, 65–93, doi:10.1016/j.jqsrt.2004.05.051, 2005.

Clerbaux, C., George, M., Turquety, S., Walker, K. A., Barret, B., Bernath, P., Boone, C., Borsdorff, T., Cammas, J. P., Catoire, V., Coffey, M., Coheur, P.-F., Deeter, M., De Mazière, M., Drummond, J., Duchatelet, P., Dupuy, E., de Zafra, R., Eddounia, F., Edwards, D. P., Emmons, L., Funke, B., Gille, J., Griffith, D. W. T., Hannigan, J., Hase, F., Höpfner, M., Jones, N., Kagawa, A., Kasai, Y., Kramer, I., Le Flochmoën, E., Livesey, N. J., López-Puertas, M., Luo, M., Mahieu, E., Murtagh, D., Néd'elec, P., Pazmino, A., Pumphrey, H., Ricaud, P., Rinsland, C. P., Robert, C., Schneider, M., Senten, C., Stiller, G., Strandberg, A., Strong, K., Sussmann, R., Thouret, V., Urban, J., and Wiacek, A.: CO measurements from the ACE-FTS satellite instrument: data analysis and validation using ground-based, airborne and spaceborne observations, Atmos. Chem. Phys., 8, 2569–2594, doi:10.5194/acp-8-2569-2008, 2008.

Di Biagio, C., Muscari, G., di Sarra, A., de Zafra, R. L., Eriksen, P., Fiocco, G., Fiorucci, I., and Fuà, D.: Evolution of temperature, O_3, CO, and N_2O profiles during the exceptional 2009 Arctic major stratospheric warming as observed by lidar and millimeter-wave spectroscopy at Thule (76.5° N, 68.8° W), Greenland, J. Geophys. Res., 115, D24315, doi:10.1029/2010JD014070, 2010.

Dupuy, E., Urban, J., Ricaud, P., Le Flochmoem, E., Lautie, N., Murtagh, D., De La Noe, J., El Amraoui, L., Eriksson, P., Forkman, P., Frisk, U., Jegou, F., Jimenez, C., and Olberg, M.: Strato-mesospheric measurements of carbon monoxide with the Odin Sub-Millimetre Radiometer: Retrieval and first results, Geophys. Res. Lett., 31, L20101, doi:10.1029/2004GL020558, 2004.

Eriksson, P., Jiménez, C., and Bühler, S. A.: Qpack, a general tool for instrument simulation and retrieval work, J. Quant. Spectrosc. Ra., 91, 47–64, doi:10.1016/j.jqsrt.2004.05.050, 2005.

Filipiak, M. J., Harwood, R. S., Jiang, J. H., Li, Q., Livesey, N. J., Manney, G. L., Read, W. G., Schwartz, M. J., Waters, J. W., and Wu, D. L.: Carbon monoxide measured by the EOS Microwave Limb Sounder on Aura: First results, Geophys. Res. Lett., 32, L14825, doi:10.1029/2005GL022765, 2005.

Forkman, P., Eriksson, P., Winnberg, A., Garcia, R. R., and Kinnison, D.: Longest continuous ground-based measurements of mesospheric CO, Geophys. Res. Lett., 30, 1532, doi:10.1029/2003GL016931, 2003.

Forkman, P., Eriksson, P., Murtagh, D., and Espy, P.: Observing the vertical branch of the mesospheric circulation at latitude 60 degrees N using ground-based measurements of CO and H_2O, J. Geophys. Res., 110, D05107, doi:10.1029/2004JD004916, 2005.

Funke, B., López-Puertas, M., García-Comas, M., Stiller, G. P., von Clarmann, T., Höpfner, M., Glatthor, N., Grabowski, U., Kellmann, S., and Linden, A.: Carbon monoxide distributions from the upper troposphere to the mesosphere inferred from 4.7 μm non-local thermal equilibrium emissions measured by MIPAS on Envisat, Atmos. Chem. Phys., 9, 2387–2411, doi:10.5194/acp-9-2387-2009, 2009.

Garcia, R. R., Marsh, D. R., Kinnison, D. E., Boville, B. A., and Sassi, F.: Simulation of secular trends in the middle atmosphere, 1950–2003, J. Geophys. Res., 112, D09301, doi:10.1029/2006JD007485, 2007.

Goldsmith, P., Litvak, M., Plambeck, R., and Williams, D.: Carbon Monoxide Mixing Ratio in the Mesosphere Derived From Ground-Based Microwave-Measurements, J. Geophys. Res., 84, 416–418, 1979.

Holton, J. R. and Alexander, M. J.: The Role of Waves in the Transport Circulation of the Middle Atmosphere, in: Atmospheric Science Across the Statopause, Geophysical Monograph 123, edited by: Siskind, D. E., Eckermann, S. D., and Summers, M. E., American Geophysical Union, 21–35, 2000.

Kasai, Y. J., Koshiro, T., Endo, M., Jones, N. B., and Murayama, Y.: Ground-based measurement of strato-mesospheric CO by a FTIR spectrometer over Poker Flat, Alaska, Adv. Space Res., 35, 2024–2030, doi:10.1016/j.asr.2005.04.099, 2005.

Künzi, K. F. and Carlson, E. R.: Atmospheric CO Volume Mixing Ratio Profiles Determined From Ground-Based Measurements of the $J = 1 \rightarrow 0$ and $J = 2 \rightarrow 1$ Emission Lines, J. Geophys. Res., 87, 7235–7241, 1982.

Labitzke, K. G. and van Loon, H.: The Stratosphere: Phenomena, History and Relevance, 1st Edn., Springer, Berlin, 1999.

Livesey, N., Read, W., Froidevaux, L., Lambert, A., Manney, G., Pumphrey, H., Santee, M., Schwartz, M., Wang, S., Cofield, R., Cuddy, D., Fuller, R., Jarnot, R., Jiang, J., Knosp, B., Stek, P., Wagner, P., and Wu, D.: Aura Microwave Limb Sounder (MLS) – Version 3.3 Level 2 data quality and description document, Tech. rep., Jet Propulsion Laboratory, California Institute of Technology, http://mls.jpl.nasa.gov/data/v3-3_data_quality_document.pdf, last access: 26 August 2011.

López-Valverde, M. A., López-Puertas, M., Marks, C. J., and Taylor, F. W.: Global and seasonal variations in middle atmosphere CO from UARS/ISAMS, Geophys. Res. Lett., 20, 1247–1250, 1993.

Manney, G. L., Schwartz, M. J., Krüger, K., Santee, M. L., Pawson, S., Lee, J. N., Daffer, W. H., Fuller, R. A., and Livesey, N. J.: Aura Microwave Limb Sounder observations of dynamics and transport during the record-breaking 2009 Arctic

stratospheric major warming, Geophys. Res. Lett., 36, L12815, doi:10.1029/2009GL038586, 2009.

Meijer, Y. J., Swart, D. P. J., Allaart, M., Andersen, S. B., Bodeker, G., Boyd, I., Braathen, G., Calisesi, Y., Claude, H., Dorokhov, V., von der Gathen, P., Gil, M., Godin-Beekmann, S., Goutail, F., Hansen, G., Karpetchko, A., Keckhut, P., Kelder, H. M., Koelemeijer, R., Kois, B., Koopman, R. M., Kopp, G., Lambert, J., Leblanc, T., McDermid, I. S., Pal, S., Schets, H., Stubi, R., Suortti, T., Visconti, G., and Yela, M.: Pole-to-pole validation of Envisat GOMOS ozone profiles using data from ground-based and balloon sonde measurements, J. Geophys. Res., 109, D23305, doi:10.1029/2004JD004834, 2004.

Melsheimer, C., Verdes, C., Buehler, S. A., Emde, C., Eriksson, P., Feist, D. G., Ichizawa, S., John, V. O., Kasai, Y., Kopp, G., Koulev, N., Kuhn, T., Lemke, O., Ochiai, S., Schreier, F., Sreerekha, T. R., Suzuki, M., Takahashi, C., Tsujimaru, S., and Urban, J.: Intercomparison of general purpose clear sky atmospheric radiative transfer models for the millimeter/submillimeter spectral range, Radio Sci., 40, RS1007, doi:10.1029/2004RS003110, 2005.

Palm, M., Hoffmann, C. G., Golchert, S. H. W., and Notholt, J.: The ground-based MW radiometer OZORAM on Spitsbergen – description and status of stratospheric and mesospheric O_3-measurements, Atmos. Meas. Tech., 3, 1533–1545, doi:10.5194/amt-3-1533-2010, 2010.

Parrish, A., de Zafra, R. L., Solomon, P. M., and Barrett, J. W.: A ground-based technique for millimeter wave spectroscopic observations of stratospheric trace constituents, Radio Sci., 23, 106–118, 1988.

Pearson, J., Müller, H., Pickett, H., Cohen, E., and Drouin, B.: Introduction to submillimeter, millimeter and microwave spectral line catalog, J. Quant. Spectrosc. Ra., 111, 1614–1616, doi:10.1016/j.jqsrt.2010.02.002, 2010.

Pumphrey, H. C., Filipiak, M. J., Livesey, N. J., Schwartz, M. J., Boone, C., Walker, K. A., Bernath, P., Ricaud, P., Barret, B., Clerbaux, C., Jarnot, R. F., Manney, G. L., and Waters, J. W.: Validation of middle-atmosphere carbon monoxide retrievals from the Microwave Limb Sounder on Aura, J. Geophys. Res.-Atmos., 112, D24S38, doi:10.1029/2007JD008723, 2007.

Raffalski, U., Hochschild, G., Kopp, G., and Urban, J.: Evolution of stratospheric ozone during winter 2002/2003 as observed by a ground-based millimetre wave radiometer at Kiruna, Sweden, Atmos. Chem. Phys., 5, 1399–1407, doi:10.5194/acp-5-1399-2005, 2005.

Remsberg, E. E., Marshall, B. T., Garcia-Comas, M., Krueger, D., Lingenfelser, G. S., Martin-Torres, J., Mlynczak, M. G., Russell, J. M., Smith, A. K., Zhao, Y., Brown, C., Gordley, L. L., Lopez-Gonzalez, M. J., Lopez-Puertas, M., She, C., Taylor, M. J., and Thompson, R. E.: Assessment of the quality of the Version 1.07 temperature-versus-pressure profiles of the middle atmosphere from TIMED/SABER, J. Geophys. Res., 113, D17101, doi:10.1029/2008JD010013, 2008.

Rodgers, C. D.: Inverse Methods for Atmospheric Sounding, World Scientific Publishing, 2000.

Rothman, L., Jacquemart, D., Barbe, A., Benner, D. C., Birk, M., Brown, L., Carleer, M., Chackerian, J., Chance, K., Coudert, L., Dana, V., Devi, V., Flaud, J., Gamache, R., Goldman, A., Hartmann, J., Jucks, K., Maki, A., Mandin, J., Massie, S., Orphal, J., Perrin, A., Rinsland, C., Smith, M., Tennyson, J., Tolchenov, R., Toth, R., Auwera, J. V., Varanasi, P., and Wagner, G.: The HITRAN 2004 molecular spectroscopic database, J. Quant. Spectrosc. Ra., 96, 139–204, doi:10.1016/j.jqsrt.2004.10.008, 2005.

Solomon, S., Garcia, R. R., Olivero, J. J., Bevilacqua, R. M., Schwartz, P. R., Clancy, R. T., and Muhleman, D. O.: Photochemistry and Transport of Carbon Monoxide in the Middle Atmosphere, J. Atmos. Sci., 42, 1072–1083, 1985.

Steck, T., von Clarmann, T., Fischer, H., Funke, B., Glatthor, N., Grabowski, U., Höpfner, M., Kellmann, S., Kiefer, M., Linden, A., Milz, M., Stiller, G. P., Wang, D. Y., Allaart, M., Blumenstock, Th., von der Gathen, P., Hansen, G., Hase, F., Hochschild, G., Kopp, G., Kyrö, E., Oelhaf, H., Raffalski, U., Redondas Marrero, A., Remsberg, E., Russell III, J., Stebel, K., Steinbrecht, W., Wetzel, G., Yela, M., and Zhang, G.: Bias determination and precision validation of ozone profiles from MIPAS-Envisat retrieved with the IMK-IAA processor, Atmos. Chem. Phys., 7, 3639–3662, doi:10.5194/acp-7-3639-2007, 2007.

Velazco, V., Wood, S. W., Sinnhuber, M., Kramer, I., Jones, N. B., Kasai, Y., Notholt, J., Warneke, T., Blumenstock, T., Hase, F., Murcray, F. J., and Schrems, O.: Annual variation of strato-mesospheric carbon monoxide measured by ground-based Fourier transform infrared spectrometry, Atmos. Chem. Phys., 7, 1305–1312, doi:10.5194/acp-7-1305-2007, 2007.

Waters, J., Froidevaux, L., Harwood, R., Jarnot, R., Pickett, H., Read, W., Siegel, P., Cofield, R., Filipiak, M., Flower, D., Holden, J., Lau, G., Livesey, N., Manney, G., Pumphrey, H., Santee, M., Wu, D., Cuddy, D., Lay, R., Loo, M., Perun, V., Schwartz, M., Stek, P., Thurstans, R., Boyles, M., Chandra, K., Chavez, M., Chen, G., Chudasama, B., Dodge, R., Fuller, R., Girard, M., Jiang, J., Jiang, Y., Knosp, B., LaBelle, R., Lam, J., Lee, K., Miller, D., Oswald, J., Patel, N., Pukala, D., Quintero, O., Scaff, D., Snyder, W. V., Tope, M., Wagner, P., and Walch, M.: The Earth observing system microwave limb sounder (EOS MLS) on the aura Satellite, IEEE T. Geosci. Remote, 44, 1075–1092, doi:10.1109/TGRS.2006.873771, 2006.

Waters, J. W., Wilson, W. J., and Shimabukuro, F. I.: Microwave Measurement of Mesospheric Carbon Monoxide, Science, 191, 1174–1175, doi:10.1126/science.191.4232.1174, 1976.

Waugh, D. W. and Rong, P.-P.: Interannual Variability in the Decay of Lower Stratospheric Arctic Vortices, J. Meteorol. Soc. Jpn., 80, 997–1012, 2002.

Waugh, D. W., Randel, W. J., Pawson, S., Newman, P. A., and Nash, E. R.: Persistence of the lower stratospheric polar vortices, J. Geophys. Res., 104, 27191–27201, doi:10.1029/1999JD900795, 1999.